Experimental Thermal and Fluid Science 142 (2023) 110825

Contents lists available at ScienceDirect

Experimental Thermal and Fluid Science

journal homepage: www.elsevier.com/locate/etfs

Engine Combustion Network "Spray G": Wall heat transfer characterization by infrared thermography

Mirko Zaccara [a,1], César Carvallo [b,*,2], Alessandro Montanaro [c,3], Jaime Gimeno [b,4], Luigi Allocca [c,5], Gennaro Cardone [a,6]

[a] University of Naples "Federico II", Department of Industrial Engineering, Naples, 80125, Italy
[b] CMT - Motores Térmicos, Universitat Politècnica de València, Valencia, 46022, Spain
[c] STEMS - Consiglio Nazionale delle Ricerche (CNR), Naples, 80125, Italy

ARTICLE INFO

Keywords:
Spray-wall interaction
Heat transfer measurements
Infrared thermography
GDI injector

ABSTRACT

Nowadays, several efforts are being made to design more efficient, cleaner, and economically accessible engines. Spray-wall interactions are strongly related with the fuel–air mixture and emission formation. As such, they are considered as the most important physical processes in engine research. In the present study, the infrared thermography coupled with an inverse heat transfer data reduction is applied to evaluate the wall heat transfer of an iso-octane spray generated by a multi-hole gasoline direct injector (Spray G) impinging on a heated thin foil. The experimental apparatus includes an Invar foil (50 μm in thickness) heated by Joule effect and the injector located at 66.66 injector nozzle diameter above the surface. Thermal images of the impinging spray are acquired from the dry side of the foil at several time delays from the start of injection at two different injection pressures (10 and 20 MPa) and two different wall temperatures (373 and 473 K). The experimental data are reduced in the dimensionless form in terms of the spray cooling efficiency ξ, which represents the ratio between the spray cooling heat flux and the heat transfer capability of the fluid, by taking into account the area of impact of the spray. Results show a substantial increment of the heat flux and the spray cooling efficiency by increasing the wall temperature. Also, the increment of the injection pressure has an increasing effect on the area of impact, the heat flux, and the efficiency of the spray for both wall temperatures investigated in the experimental campaign. The spray cone angle and the plume jet axis angle were also estimated from the wall heat flux distribution.

1. Introduction

Great efforts are underway in the field of internal combustion engines devoted to increasing the combustion efficiency coupled to the reduction of the pollutant emissions to safeguard community health. A good efficiency of the combustion process goes through an improvement of the air/fuel mixture preparation before the start of the ignition that, for injected supplying fuel, means a rapid fragmentation of the liquid bulk in smaller and smaller droplets, their rapid vaporization and homogeneous mixing with the air in the combustion chamber. Increasing the injection pressure is an efficient way to obtain finer fuel droplets though, at typical pressures of 20–100 MPa, the spray penetration increases, and additional troubles overcome due to the deposit of fuels on the chamber wall [1]. Several efforts are being used to design more efficient, cleaner and economical engines. To achieve this goal, the fuel injection process, spray development and combustion are being studied using computational and experimental approaches [2–5]. It is well known that there are aspects of the fuel injection process, specifically, of the spray-wall interaction (SWI) that need to be understood and improved. The spray-wall interaction phenomenon on combustion process is considerably complex, as different behaviors of the droplets can be identified leading to a fuel film formation on the walls after

* Corresponding author.
E-mail address: cecargar@posgrado.upv.es (C. Carvallo).
[1] Ph.D., University of Naples "Federico II", Department of Industrial Engineering, Piazzale Tecchio 80.
[2] Ph.D. Student, CMT - Motores Térmicos.
[3] Researcher, STEMS - CNR, Via Guglielmo Marconi 4.
[4] Associate Professor, CMT - Motores Térmicos.
[5] Senior Researcher, STEMS - CNR, Via Guglielmo Marconi 4.
[6] Full Professor, University of Naples "Federico II", Department of Industrial Engineering, Piazzale Tecchio 80.

https://doi.org/10.1016/j.expthermflusci.2022.110825
Received 8 June 2022; Received in revised form 29 November 2022; Accepted 1 December 2022
Available online 10 December 2022

Nomenclature

Acronyms

CFD	Computational Fluid Dynamics
ECN	Engine Combustion Network
FPA	Focal plane array
GDI	Gasoline direct injection
IR	Infrared
NETD	Noise equivalent temperature difference
SWI	Spray-wall interaction

Variables

α	Thermal diffusivity coefficient
ΔH_{fg}	Heat of vaporization of the fluid
ΔT	Temperature drop
δ_{invar}	Invar thickness
δ_{paint}	Paint thickness
$\dot{m}$	Mass flow rate
ϵ	Emissivity
ρ_{invar}	Invar density
ρ_{paint}	Paint density
ρ_{tp}	Density
σ	Boltzmann constant
θ	Spray cone angle
ξ	Spray cooling efficiency
c_p	Specific heat at constant pressure
c_{p_v}	Constant pressure heat capacity of gas
d_0	Injector nozzle diameter
dc	Footprint to spray center distance
k_{invar}	Invar thermal conductivity
k_{paint}	Paint thermal conductivity
L	Length of the plate
Nu	Nusselt number
p_{inj}	Injection pressure
q_r	Radiative heat flux
q_t	Tangential conduction heat flux
q_{joule}	Joule heat flux
q_{nc}	Natural convection heat flux
q_{spray}	Heat flux
R^2	Coefficient of determination
T_1	Lower wall temperature
T_f	Fuel temperature
T_L	Leidenfrost temperature
T_m	Thin foil mean temperature
T_w	Upper wall temperature
$T_{1_{num}}$	Numerically obtained T_1
T_f	Spray impact temperature
T_{sat}	Saturation temperature
t	Time
IT	Integration Time

the spray interaction, increasing the unburned hydrocarbons and soot formation.

Regarding engine efficiency, the heat transfer between the fuel deposits and the walls in the cylinder produces an unwanted heat loss and less engine efficiency. It is known that the spray-wall impact promotes the breakup of the droplets, reducing their size, accelerating the evaporation and the combustion process, while the dispersion of the spray in the wall reduces the local spray temperature and may delay the ignition [6–9].

It is important to highlight this phenomenon because, for direct injection engines under cold start conditions, in which there are low densities and temperatures, those conditions promote a large liquid spray penetration that might reach the piston surface or the walls of the combustion chamber. Even the computational models are powerful tools, its accuracy relies on the existence of high-quality experimental data, a reason why several efforts are being taken in place by different research institutes. Heat transfer measurements are required to widen the fundamental knowledge on the spray-wall interaction and to serve as a database for models improvement.

For gasoline direct injection engines, the spray-wall interactions are among the most interesting physical processes nowadays because they play an important role in the process of mixture formation. Those interactions could produce fuel deposits on the surface of the piston because there is not sufficient time for the fuel to completely evaporate. In this complex phenomenon, different parameters have a strong influence like the distance between the injector tip and the wall, the spray cone angle, the fuel temperature, wall temperature, wall-fuel difference in temperature, the number of consecutive injections, and the injection pressure itself. In particular, the injection pressure and the wall/fuel difference in temperature have an important influence on the SWI. More experimental data related to the time-dependent temperature on the piston surface could make the current knowledge about droplet/wall interactions stronger.

To analyze the SWI it is important to have a clear sight of what the spray cooling phenomenon is. This phenomenon takes place when liquid forced through a small orifice (injector holes) splits into a scattering cloud of fine droplets and then impacts on a heated surface [10]. Once the droplets reach the surface they can evaporate or form a thin liquid film, removing huge amounts of energy at low temperature due to the latent heat of evaporation in addition to the energy needed to produce the phase change of the liquid.

It is possible to find studies about one single droplet interaction with walls like the one presented by Moreira et al. [11]. The issue is related to the fact that a spray does not behave exactly as the addition of individual droplets. In fact, a directly injected spray is defined by strong spatial and temporal interactions resulting in a complex physical phenomenon that cannot be fully explained by single droplet studies. As a result, it is important to acquire experimental data related to spray-wall interaction using real sprays impacting on piston-like surfaces.

Qualitative measurements have been conducted on real sprays applying optical techniques as Schlieren imaging [12–14], Mie scattering technique [13,15,16], Planar laser-induced fluorescence [17] and Phase Doppler Anemometry technique [18]. Those methodologies are useful to acquire information about the propagation and the chemical composition of the spray before and after the beginning of the wall interaction but they do not give any information about the temperature drop and the footprint after the spray wall impingement.

As stated before, CFD studies are carried out to understand the physics behind the multi-phase sprays propagation and evaporation [18–20] and, in addition to experimental contributions [21–23], they are providing enough information to clarify the physics behind the spray development.

The “Spray G” injector, an eight-hole solenoid-activated gasoline-direct injector, has been identified by the ECN Engine Combustion Network (ECN) as a benchmark for the gasoline direct injectors (GDI) in order to develop a data-set of experiments and computational fluid dynamics simulations which will become a focal point for models validation and further advanced diagnostics [24].

Infrared Thermography (IR) has been already employed to visualize and measure the temperature distribution of impinging sprays [25,26]. This technique brings several advantages [27] that make it suitable in such a complex area of investigation: it provides high sensitivity

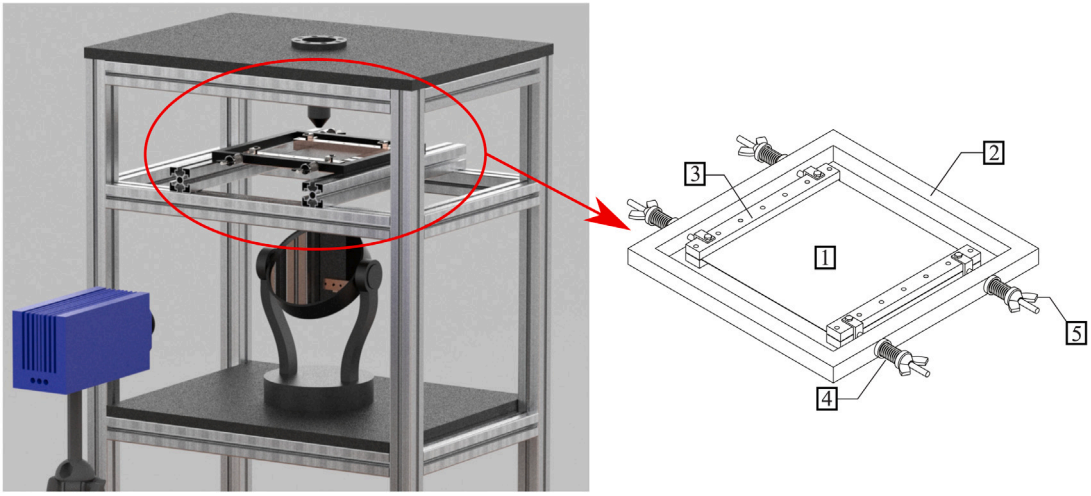

Fig. 1. Rendering of the experimental apparatus with the detailed drawing of the clamped thin foil that includes the following components: 1. Invar thin foil 2. Square rigid frame 3. Copper clamp 4. Spring 5. Holding nut.

measurements and it is a non-intrusive, two-dimensional technique capable of very low response time. Gibbons and Robinson [28] carried out, for the first time, a study of a single source electrospray using thin foil thermography to investigate the local convective heat transfer. A preliminary study employing IR thermography to study the "Spray G" wall interaction with hot wall was performed by Contino et al. [29]. The latter was focused mainly on the experimental setup and the relative infrared camera calibration procedure. Moreover, the temperature maps presented and discussed are relative to high time delay from the start of injection (up to 20 ms), when the interaction is ended (injection duration 1 ms). Even though the "Spray G" injector has been largely characterized in previous works as reported by Duke et al. [30], no heat transfer measurements are available in the literature. In the present work, using the same experimental apparatus described in [29], the wall heat transfer interaction was investigated by means of infrared thermography coupled with an inverse heat transfer data reduction.

In the first place, the experimental data reduction and the heat flux calculation methodology are described in detail. Then, the results are presented and discussed in terms of the spray area of impact and the non-dimensional spray cooling efficiency distribution. Finally, the heat transfer data are also used to evaluate the spray cone angle and the plume jet axis angle.

2. Experimental setup

A render of the experimental setup used to evaluate the time history of the wall temperature and the heat transfer of a spray impacting on an electrically heated thin foil is shown in Fig. 1 [29]. As it can be noticed in Fig. 2 the apparatus can be divided in two different sub-systems: the spray injection/impinging wall and the acquisition system.

The ECN injector eight-hole nozzle (d_0 = 165 μm) are equally spaced on a circumference. As commonly seen in GDI applications, the nozzle holes are stepped and thus a 388 μm counterbore was machined coaxially with each of the eight inner holes. The complete technical description of the adopted injector is reported in [30–32]. The details of the spray geometry are described in Fig. 3. Due to the nozzle tip counterbore, the Coanda effect produces a deviation of the spray from the drill hole design axis.

The spray impingement characterization is carried out by using a target plate reported in Fig. 1. It is a squared, 100 mm in side, Invar foil (Goodfellow FE02-FL-000140) of 50 μm in thickness included within an aluminum rigid frame electrically insulated and clamped between two copper clamps. A current controlled DC power supply allows to set a specific amperage between the two sides of the target plate which, in turn, is uniformly and steadily heated by Joule effect. For the present work, the tests are performed with two wall temperatures of 373 and 473 K, which are obtained with the current application of 31.2 and 53.2 A through the foil respectively, resulting in a voltage drop of 1.17 and 1.92 V.

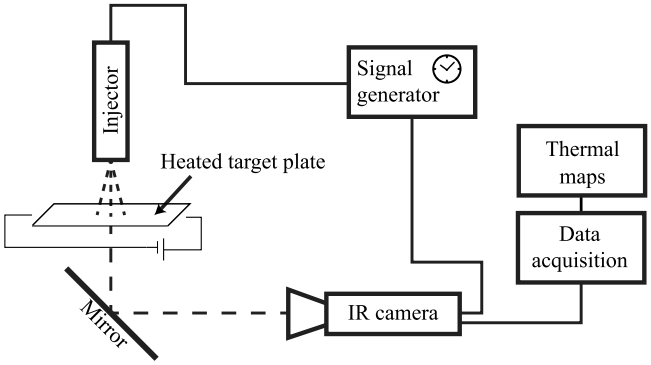

Fig. 2. Schematic of the experimental setup.

A continuous tension stress is applied through four springs and holding nuts to keep the foil straight during heating and to avoid the thermal expansion effects. The target plate is located at z = 11 mm, corresponding to z/d_0 = 66.66, downstream of the injector tip and facing the injector's axis perpendicularly to minimize the natural convection effects on the foil.

The IR thermal camera and the digital signal generator represent the whole data acquisition and control system. The IR camera employed in the present work is the Cedip JADE III, a focal plane array (FPA) camera with spectral response in the 3-5 μm infrared band, noise equivalent temperature difference (NETD) of 25 mK at 298 K, InSb sensor dimensions equal to 320 × 240 pixel, and a maximum acquisition frame rate of 170 Hz. A cropped sensor (160 × 120 pixel) has been employed during acquisition for data bandwidth issues resulting in a spatial resolution of 3.05 pixel/mm. Two IR camera integration times (IT) are employed for the two investigated wall temperatures: 150 μs (T_w = 373 K), 30 μs (T_w = 473 K). It is worth noting that the ITs have been chosen to maximize the IR camera thermal sensitivity in the selected temperature range. As it can be noted in Figs. 1 and 2, the IR camera acquires the radiations deviated by a first surface mirror which has been interposed for safety reasons. Since the latter absorbs part of the radiations, an in situ camera calibrations by using

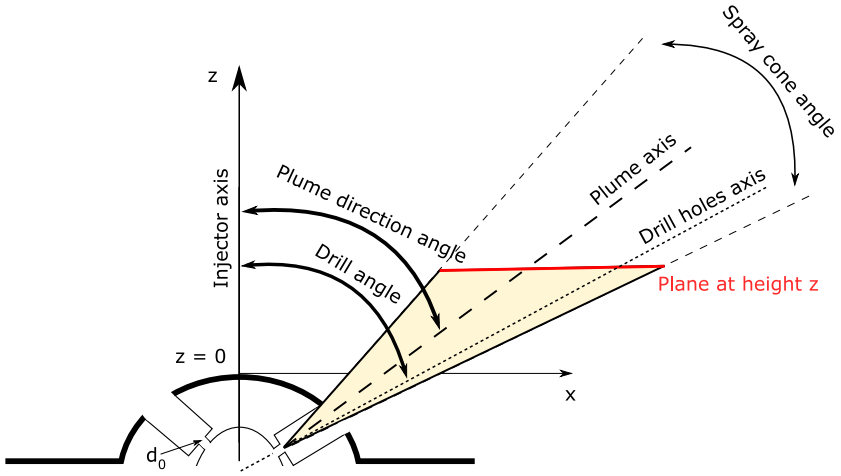

Fig. 3. Spray G single plume geometry.

a blackbody [27] have been conducted by respecting the optical path employed during the experimental tests. Further details on the camera calibration procedure are reported in Contino et al. [29]. In order to improve the accuracy of the thermal measurements, the dry side of the foil is painted with a high emissivity black paint ($\epsilon = 0.95$).

Iso-octane has been employed as a single-component fuel surrogate for gasoline. For the present work, the injection duration has been set to 1 ms and two different injection pressures of 10 and 20 MPa have been investigated. Furthermore, both the injector and the fuel temperature operate at room temperature (298 K) and all the tests are carried out in an open environment at room temperature (298 K) and atmospheric pressure (0.1 MPa). Under direct injection strategies, the wall wetting phenomenon is quite common, followed by poor evaporation of the fuel film adhered to the piston surface. This phenomenon is more pronounced under engine cold-start conditions because of the low cylinder temperature. Also, when the wall surface is at a lower temperature than the saturation temperature of the fuel results in significant film formation. For our case study, the 373 K temperature was selected to reproduce a cold-start engine condition, and the 473 K temperature was selected to use a higher temperature than the Nukyama and Leidenfrost temperature of the isooctane.

Since the studied phenomenon is faster than the maximum acquisition rate of the IR camera, the time-history of the wall spray cooling is reconstructed by a single-image acquisition delayed with respect to the start of the injection and repeating the spray shots. In particular, the injector frequency is fixed to 0.0625 Hz which corresponds to 16 s of time interval between one shot and the next one in order to recover the initial wall temperature between them. A BNC-575 digital delay/pulse generator has been employed to synchronize the injection start ($t = 0$ s) and the IR camera acquisition delay steps every 50 µs from 0 to 1.2 ms, and every 100 µs up to 1.8 ms. To improve the accuracy of the measured data, 125 repetitions of the spray impact were carried out for each time delay step.

The details of the operating conditions are summarized in Table 1.

Table 1
Investigated operating conditions.

Test conditions		
Thin foil temperature (T_w)	[K]	373 ± 2, 473 ± 2
Current through the foil	[A]	31.2 ± 0.15 , 53.2 ± 0.27
Voltage drop through the foil	[V]	1.17 ± 0.01, 1.92 ± 0.01
Injection pressure (p_{inj})	[MPa]	10 ± 0.5, 20 ± 0.5
Nozzle-to-wall distance	[mm]	11 ± 0.01
Fuel		iso-octane (C_8H_{18})
Fuel temperature (T_f)	[K]	298 ± 2
Injected fuel mass	[mg]	10.48 @ $p_{inj} = 10$ MPa
		15.44 @ $p_{inj} = 20$ MPa
Spray duration	[ms]	1
Ambient temperature	[K]	298 ± 0.5
IR camera settings		
Detector format	[pixel]	half cropped: 160 × 120
Spatial resolution	[pixel/mm]	3.05
Integration time (IT) @$T_w = 373$ K	[µs]	150
Integration time (IT) @$T_w = 473$ K	[µs]	30
Iso-octane thermophysical properties		
Density @25 °C	[kg/m^3]	690
Specific heat at constant pressure @15.6 °C	[J/g °C]	2.047
Dynamic viscosity @20 °C	[mPa s]	0.503
Saturation temperature (T_{sat})	[K]	372
Enthalpy of vaporization (ΔH_{vap})	[kJ/mol]	38.2
Specific heat	[J/mol K]	239.1
Leidenfrost Temperature (T_L)	[°C]	175 ± 5
Nukiyama Temperature (T_N)	[°C]	119 ± 1

3. Data post-processing

In this section, the methodologies adopted to extract the information from the thermal images acquired in the experimental campaign are presented. The section is divided into five subsections: the temperature measurements, the heat flux calculations, the area of impact evaluation, the spray cooling efficiency and the plume jet axis and the spray cone angle.

3.1. Temperature measurements

A typical delay step temperature drop of the dry side ΔT map obtained by averaging the 125 acquired temperature images after subtracting the one at $t = 0$ s is reported in Fig. 4.

As it can be noted, the plume shapes present a slight non-uniformity which can be ascribed to a difference in the holes diameters and discharge coefficients [30]. As a result, a post-process has been applied to the temperature drop maps consisting in a rotation around the injector's axis and a 45-degree sector symmetrization to reduce the plume to plume temperature variation. The rotation center has been identified as the center of a least square circumference which fits the barycentre of each plume after applying a threshold close to the maximum. An example of a post-processed temperature map is shown in Fig. 5. The injector nozzle diameter d_0 has been used for the axes normalization.

The time history of the temperature drop of the stagnation spray impact point, which coincides with the maximum temperature drop point, is reported in Fig. 6 for each investigated condition. Since the

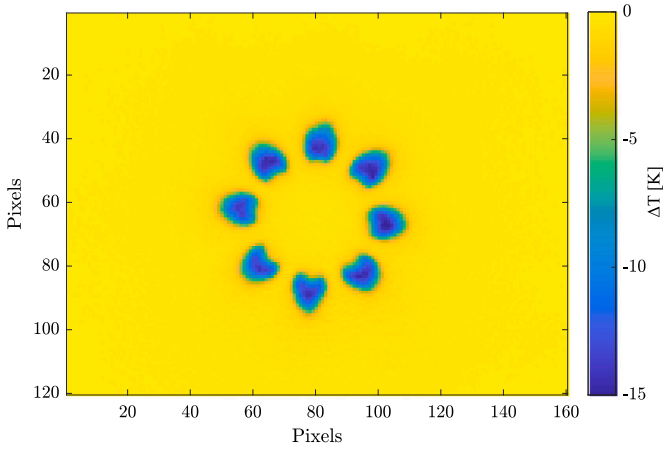

Fig. 4. Average temperature drop map for $p_{inj} = 20\,\text{MPa}$, $T_w = 473\,\text{K}$ and $t = 0.9\,\text{ms}$.

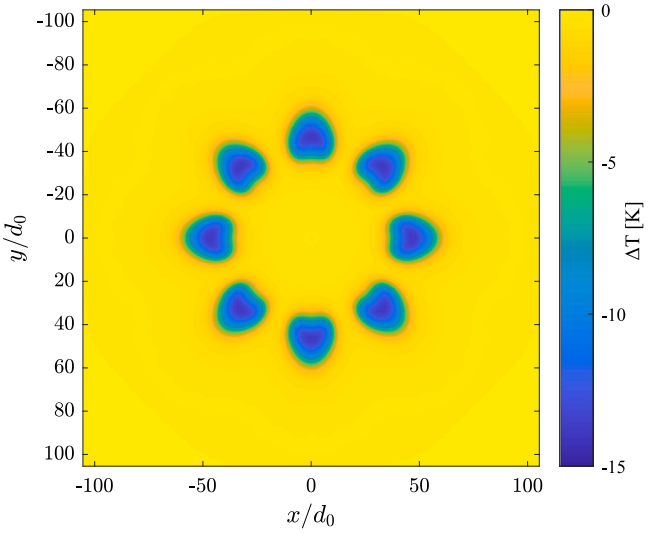

Fig. 5. Post-processed temperature drop map for $p_{inj} = 20\,\text{MPa}$, $T_w = 473\,\text{K}$ and $t = 0.9\,\text{ms}$.

IR camera measures the back temperature of the target plate, the first significant temperature drop is obtained only after 0.4 ms from the injection start. This delay is due to the time needed from the spray to reach the plate and to the thermal inertia of the foil which does not allow the thermal wave to instantaneously propagate from the front to the back surface [33].

As it can be seen, the higher the wall temperature of the foil, the higher the temperature drop obtained after the impingement. This behavior is related to the strong influence of the wall temperature on the vaporization of the fuel. On the other hand, by fixing the wall temperature, the injection pressure contribution has fewer effects on the temperature drop. It is worth noting that the condition at $p_{inj} = 20\,\text{MPa}$ and $T_w = 473\,\text{K}$ exhibits a change in the temperature drop trend for the time interval from 1 ms to 1.3 ms. Such a behavior could be ascribed to small changes in the ambient temperature and the IR camera temperature during the data acquisition. However, these measurement points are not taken into account for the heat flux calculation described later in Section 3.2.

3.2. Heat flux

To increase the heat transfer evaluation accuracy and robustness an Inverse Heat Transfer Problem (IHTP) was implemented [34]. For each pixel (x, y coordinate) of the recorded thermal image the spray wall heat flux q_{spray} is computed assuming one dimensional temperature distribution across target plate (slab). Due to the short measuring time (Fourier number <1), also if the Biot number is ≪1, the slab cannot be assumed thermally thin [33]. A sketch of the slab model with all acting heat fluxes, is presented in Fig. 7. The slab is composed of two materials (Invar and black paint with thickness δ_{invar} and δ_{paint} respectively). The thermal conductivity of Invar was assumed temperature dependent according to [35] while the thickness and the remaining thermal physical properties were defined using the supplier data sheet. The paint thermal physical properties were determined from the data of Raghu and Philip [36], while the paint thickness was measured using Fisher Dualscope MPOR-FP. The foil and paint properties are outlined in Table 2.

In the following T_w, is the temperature of the upper wall and T_1 is the temperature of the lower wall. The test run time $[0, t_f]$ can be divided in two phases: the spray start-up (the time required from the spray to reach the wall plus the time required to the spray jet to be completely developed) and the quasi-steady phase where the spray wall heat flux is steady. These two phases are indicated hereinafter as $[0, t_i]$ and $[t_i, t_f]$. Different heat fluxes are present on the upper wall: the spray wall heat flux q_{spray} (assumed equal zero in $[0, t_i]$ and constant in $[t_i, t_f]$), natural convection heat flux q_{nc} and radiative heat flux q_r. On the lower wall only the natural convection and radiative heat flux are present. The Invar slab part is also heated by Joule effect q_{joule} as described in the experimental apparatus. The radiative flux for the upper wall is computed as $q_r = \sigma \cdot \epsilon_{invar} \cdot (T_w^4 - T_{amb}^4)$, while at lower wall $q_r = \sigma \cdot \epsilon_{paint} \cdot (T_1^4 - T_{amb}^4)$ where σ is the Stefan–Boltzmann constant. The natural convection heat flux at the upper wall is $q_{nc} = h_{up} \cdot (T_w - T_{amb})$ while at lower wall $q_{nc} = h_{down} \cdot (T_1 - T_{amb})$. For an horizontal plate, the Nusselt number for the natural convection with exchange on the upper side is $Nu = 0.54 \cdot (Gr \cdot Pr)^{1/4}$ while with exchange on the lower side is $Nu = 0.27 \cdot (Gr \cdot Pr)^{1/4}$ [37]. As such, it can be assumed $h_{up} = 2 \cdot h_{down}$. Up to time t_i, the temperature across the slab was assumed constant in time and equal to the temperature $T_{1_{exp}}$ measured by the infrared camera. Then, by making an energy balance in the phase $[0, t_i]$ between the measured q_{joule}, q_{nc} and q_r on upper and lower wall, it is possible to compute the natural convection heat transfer coefficient h_{up} and h_{down}. Due to the small temperature variation, the h_{up} and h_{down} will be assumed constant during the next phase.

In the phase $[t_i, t_f]$ the transient one-dimensional Fourier heat equation in the slab is solved with a finite difference method based on the Crank-Nicholson scheme that guarantees a second order accuracy in both space and time without high computational burden. An initial guess of the heat conduction solution is formulated by an arbitrary spray heat flux. Then, the calculated back surface temperature solution ($T_{1_{num}}$) is compared to the measured one ($T_{1_{exp}}$) in a least-square sense. The function

$$R(q_{spray}, t_i) = \int_{t_i}^{t_f} \cdot \left[T_{1_{num}}(t - t_i) - T_{1_{exp}}(t) \right]^2 dt \quad (1)$$

is used as an objective functional to be minimized through a proper optimization scheme by updating the heat flux guess until convergence is reached. The optimization procedure is based on the trust-region-reflective algorithm [38]. In the present data reduction tf was limited to 1.05 ms, that is less of spray duration (1 ms) plus time required from spray to reach the wall (0.113–0.126 ms), when the spray was still active. It should be noted also that the terms q_{joule}, q_{nc} and q_r are very small respect q_{spray} at the stagnation point (typically 0.1%). These latter terms influence the data reduction essentially in the region of low q_{spray}.

In Fig. 8, the typical experimental and optimized numerical temperature drop obtained by the Fourier equation hereinafter have been compared in four different point of coordinates. As it can be noted the experimental and numerical data are in good agreement, as illustrated by the determination coefficient values. Most importantly, in the presence of strong spatial temperature gradients, 1D techniques

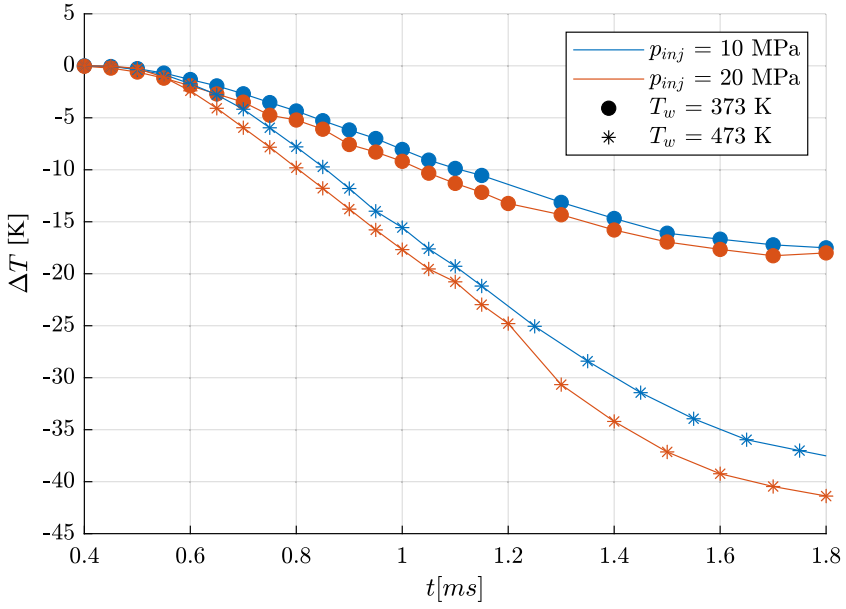

Fig. 6. Temperature drop curves of the stagnation points over time.

Table 2
Foil and paint properties.

	Invar			Paint		
Thickness	δ_{invar}	50 ± 5	μm	δ_{paint}	10.2 ± 1.6	μm
Density	ρ_{invar}	8000 ± 80	kg m^{-3}	ρ_{paint}	1303 ± 39	kg m^{-3}
Thermal conductivity	k_{invar}	21.7 ± 0.22 @373K 42.1 ± 0.42 @473K	W m^{-1} K^{-1}	k_{paint}	0.74 ± 0.02	W m^{-1} K^{-1}
Specific heat	Cp_{invar}	515 ± 10	J kg^{-1} K^{-1}	Cp_{paint}	2557 ± 230	J kg^{-1} K^{-1}
Emissivity	ϵ_{invar}	0.15 ± 0.01	–	ϵ_{paint}	0.95 ± 0.01	–

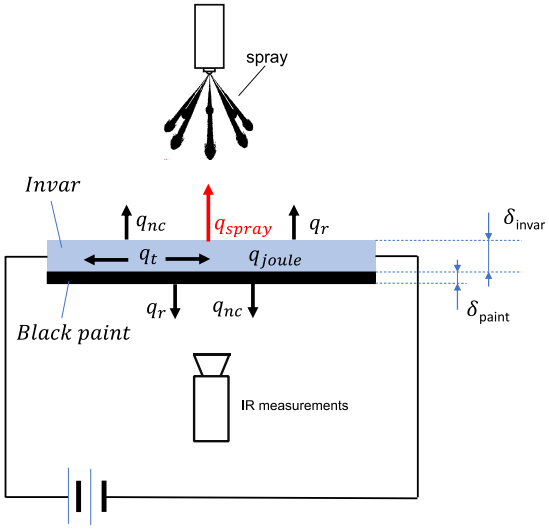

Fig. 7. A sketch of the slab model with all acting heat fluxes.

may underestimate the heat flux by neglecting the effects of lateral conduction q_t [28,39,40]. To prove that q_t is negligible in the present tests, thanks to the computed temperature distribution along the slab, first order tangential conduction heat flux is estimated by the following relationship

$$q_t = -k_{invar} \cdot \delta_{invar} \cdot \left(\frac{\partial^2 \overline{T_{invar}}}{\partial^2 x} + \frac{\partial^2 \overline{T_{invar}}}{\partial^2 y} \right) - k_{paint} \cdot \delta_{paint} \cdot \left(\frac{\partial^2 \overline{T_{paint}}}{\partial^2 x} + \frac{\partial^2 \overline{T_{paint}}}{\partial^2 y} \right) \quad (2)$$

where $\overline{T_{invar}}$ and $\overline{T_{paint}}$ are the average temperature along the slab in the Invar and paint parts respectively at final time t_f when q_t is maximum.

In 9(a), the tangential conduction heat flux distribution limited to the spray impact area (see Section 3.3) is presented for the test condition p=20 MPa and Tw=473 K, in which the maximum values of q_t are detected. As it can be noted, the absolute maximum values are measured on the borders of the impact area and on the two sides of the stagnation points where the temperature gradient is maximum. In 9(b) is also presented the percentage tangential conduction error $\tau = \frac{|q_t|}{q_{spray}} \cdot 100$ map which is at worst equal to 2.7%, with an average value of 0.66% and 0.45% in the stagnation point confirming the negligibility of the tangential conduction.

3.3. Area of impact

Different solutions to correctly identify the spray area of impact from the heat flux maps were analyzed. The approach that has shown the better agreement with flow visualizations (not shown herein) was the Otsu's method [41,42], which is based on an automatic threshold analysis by maximizing the inter-class variance of the image's Black to obtain the best separation of its interest regions. In Fig. 10, the methodology is applied and the results shown are related to the test configuration at p_{inj} = 10 MPa and T_w = 473 K. Fig. 10(a) reports the heat flux map before the segmentation; Fig. 10(b) shows the area of impact region calculated using the Otsu's method and its accuracy can be checked by overlapping the two previous images (Fig. 10(c)).

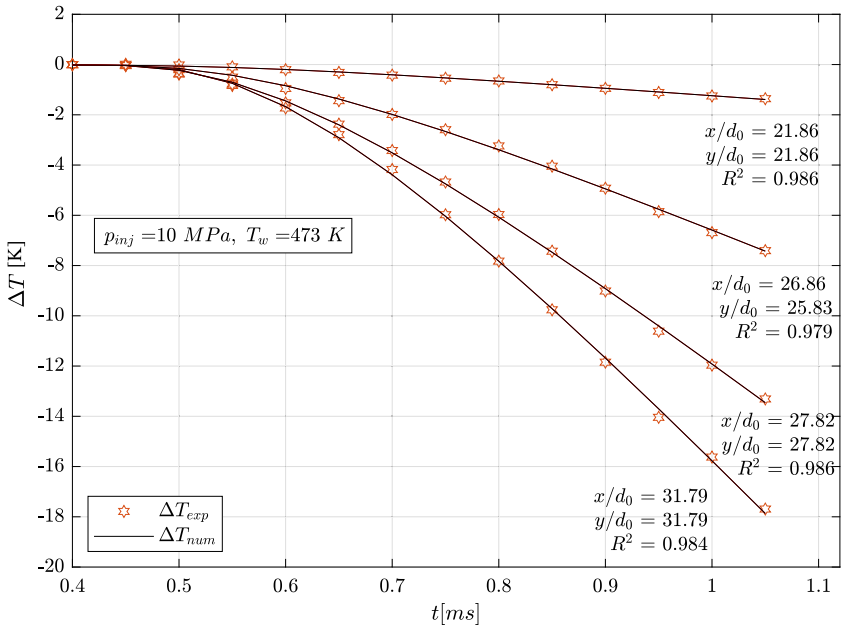

Fig. 8. Comparison between the measured and the numerically computed temperature (from the inverse heat transfer model) for p_{inj} = 10 MPa *and* T_w = 473 K.

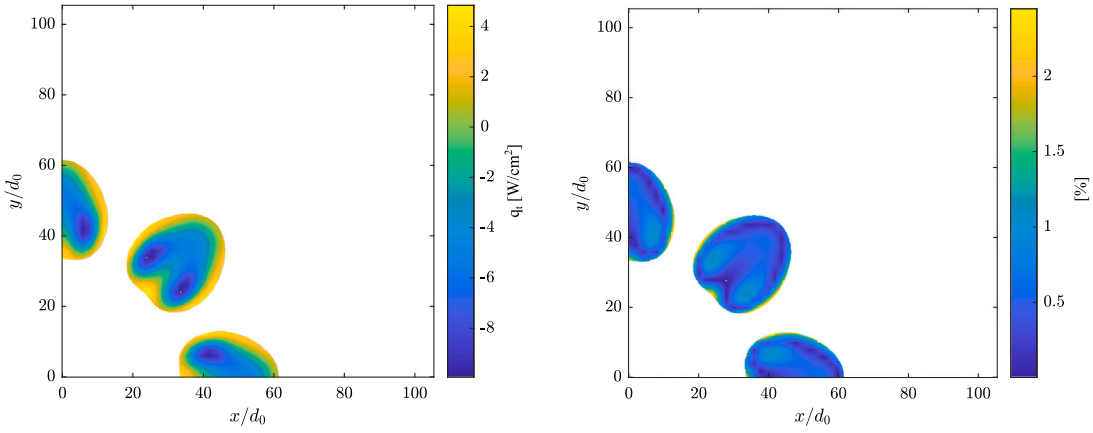

(a) Tangential conduction heat flux q_t

(b) Tangential conduction error

Fig. 9. Tangential conduction heat flux distribution limited to the spray impact area for p_{inj} = 20 MPa, T_w = 473 K.

3.4. Spray cooling efficiency

The measured heat flux data is reduced in the dimensionless form in terms of the spray cooling efficiency $\xi(x, y)$ defined as [10]

$$\xi(x,y) = \frac{q_{spray}}{\frac{\dot{m}}{A_i}\left[c_{p_l}\left(T_{sat} - T_f\right) + \Delta H_{fg}\right]} \tag{3}$$

which represents the ratio between the spray cooling heat flux and the heat transfer capability of the fluid. In fact, it takes into account the sensible heating of the liquid from the spray temperature (T_f) to the saturation temperature (T_{sat}) and the heat required to vaporize the liquid (ΔH_{fg}). Furthermore, when the temperature (T_w) is above the saturation one, the vapor generated at the surface can be superheated to the foil temperature (ΔT_{sat}) and thus the spray cooling efficiency is more precisely defined as follows

$$\xi(x,y) = \frac{q_{spray}}{\frac{\dot{m}}{A_i}\left[c_{p_l}\left(T_{sat} - T_f\right) + \Delta H_{fg} + c_{p_v}\left(T_w - T_{sat}\right)\right]} \tag{4}$$

Where $\dot{m}$ represents the mass flow rate, A_i the impact area, the term $c_{p_l}\left(T_{sat} - T_f\right)$ corresponds to the sensible heating of liquid from the spray temperature to the saturation one, ΔH_{fg} is the heat of vaporization of the fluid and the term $c_{p_v}\left(T_w - T_{sat}\right)$ is related to the vapor super-heating, and it is formed by the constant pressure heat capacity of gas (c_{p_v}), the wall temperature (T_w) and the saturation temperature. The c_{p_v} value was obtained through an interpolation process of the data reported in [43].

In order to better compare the different tested conditions, the impact area-averaged spray cooling efficiency $\bar{\xi}$ is evaluated as follows:

$$\bar{\xi} = \frac{1}{A_i}\int_{A_i} \xi(x,y)\, dA \tag{5}$$

and the relative mean absolute deviation σ_ξ, chosen as non-uniformity index of the spray cooling efficiency [44] computed as:

$$\sigma_\xi = \frac{\frac{1}{A_i}\int_{A_i} |\xi(x,y) - \bar{\xi}| dA}{\bar{\xi}} \tag{6}$$

3.5. Plume jet axis and spray cone angle evaluation

The plume direction angle β and the spray cone angle θ are obtained with a geometrical reconstruction approach, by making use 3D

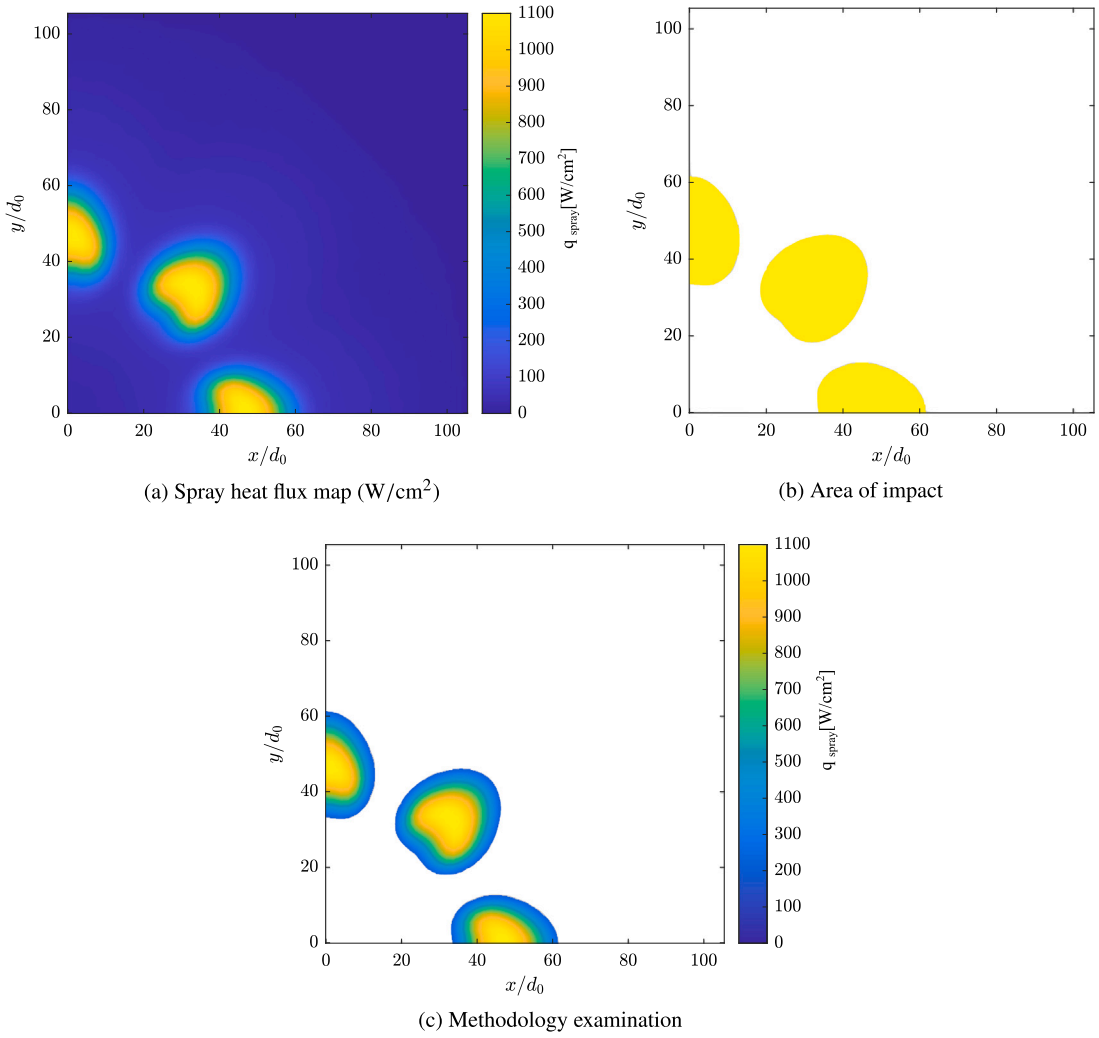

Fig. 10. Area of impact determination methodology for $p_{inj} = 20\,\text{MPa}, T_w = 473\,\text{K}$.

geometry of the "Spray G" injector (available in ECN website [24]) and the wall heat flux distribution. The position of the maximum heat flux in the impinging area and the origin of jet are used to estimate the angle β assuming that plume jet axis is the line joining these two points. To increase the accuracy identification of the maximum position (with subpixel resolution) the heat transfer data near maximum was fitted with a gaussian function. The spray cone angle θ was estimated by using a similar geometrical approach assuming that it is equal to the angle between the two lines starting from the origin of jet and that end at the extremity of the minor axis of the elliptical like shape spray area of impact.

3.6. Uncertainties analysis

The typical values and uncertainties of the parameters involved in the measurement process are reported in Tables 2 and 3. Considering such uncertainties and the error analysis of Moffat [45] and Crowder et al. [46], the estimated error in the worst case for the spray heat flux q_{spray} is less than ±9.6%, for the angle θ is less ± 0.5°, for the angle β is less ± 1°. The error analysis for A_i, ξ was not performed but the error should be very close to ± 9.6%. It is worth noting that all these uncertainties are based on a 95% confidence level.

4. Results

In the first part of this section, the results of the "Spray G" injector in terms of heat flux, spray cooling efficiency and impact area as zero-dimensional data (average, maximum and mean absolute deviation) together with an injector angles characterization are first reported and discussed. These data are reported in Table 3 with other variables such as the wall temperature against the Leidenfrost temperature (T_L), and the ΔT_{sat} as they play an important role in the physical interpretation of the results, each row of the table corresponds to each pair of pressure and temperature tested in the experimental campaign. Secondly an analysis of the two-dimensional distributions of the same results is also presented.

From Table 3 it is possible to notice that the increase in the injection pressure for the lower wall temperature (373 K) produces a change over the area of impact of 33% and a change over the maximum spray cooling efficiency and the maximum heat flux of 5%. On the other hand, for the higher wall temperature (473 K) the increment in the injection pressure produces an 14% increment in the area of impact and a 3% increment for the maximum spray cooling efficiency and the maximum heat flux. The increase in the wall temperature for the lower injection pressure (10 MPa) produces a reduction in the area of impact of 31%, and an increase over the maximum spray cooling efficiency

Table 3
Summary of zero-dimensional results.

Conditions	Results										Spray parameters		
10 MPa 473 K	1.15	9.11	1089.9	583.97	73.11	0.34	0.18	0.023	17.3	31.9	$\dot{m}$ = 10.48 [g/s]	1.05	101
10 MPa 373 K	1.67	6.28	513.71	270.22	35.26	0.16	0.08	0.011	17.8	31.6		0.83	0
	A_i [cm^2]	$\frac{\dot{m}}{A_i}$ [g/cm^2 s]	q_{max} [W/cm^2]	$\bar{q}$ [W/cm^2]	δ_q	ξ_{max}	$\bar{\xi}$	σ_ξ	θ	β		$\frac{T_w}{T_L}$	ΔT_{sat} [K]
20 MPa 373 K	2.5	6.18	542.54	223.41	41.39	0.17	0.07	0.013	19.5	32.5	$\dot{m}$ = 15.44 [g/s]	0.83	0
20 MPa 473 K	1.33	11.61	1122.9	620.26	64.91	0.35	0.19	0.02	17.3	32.9		1.05	101

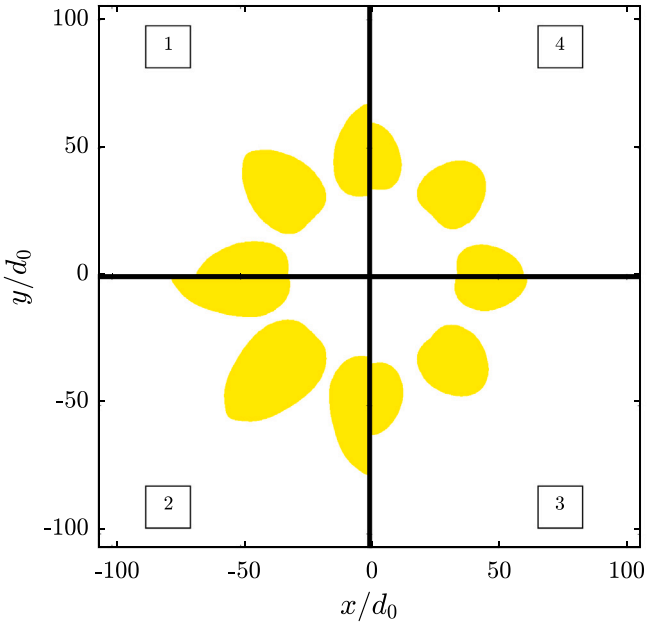

Fig. 11. Spray impact area. (1) T_w = 373 K, p_{inj} = 10 MPa, (2) T_w = 373 K, p_{inj} = 20 MPa, (3) T_w = 473 K, p_{inj} = 20 MPa, (4) T_w = 473 K, p_{inj} = 10 MPa.

and the maximum heat flux of 52%. For the higher injection pressure (20 MPa), the increase of the wall temperature produces a reduction in the area of impact of 47% and the same increment of 52% over the maximum spray cooling efficiency and the maximum heat flux. At lower wall temperature the percentage increase of the impact area is higher of the percentage increase of the injected fuel mass (+90% vs +47%), indicating a worsening of the heat exchange mechanism showed also by the decrease of average spray efficiency ξ. On the contrary, at higher wall temperature the percentage increase of the impact area is significantly lower of the percentage increase of the injected fuel mass (+18% vs +47%) indicating an improvement of the heat exchange mechanism showed by the increase of average ξ. The non-uniformity distribution of the heat flux and the spray cooling efficiency follows the same trends stated in the previous paragraphs. By keeping the same injection pressure but increasing the wall temperature an higher non-uniformity distribution value is obtained. More, by increasing the injection pressure keeping the wall temperature constant produces an increase in the non-uniformity distribution value. The heat flux and the spray cooling efficiency mean values are almost the half of the maximum values. As the heat flux peak value is located in the spray impact point, the heat flux in the area of impact has an important variability as the distance with the impact point increases. More heat transfer occurs where the major amount of liquid is in contact with the heated wall. For the measured conditions, the heat flux, the mass flow rate and the area of impact are varying. This mean that a combined contribution is taking part over the final spray cooling efficiency value obtained by using the (4). The spray cooling efficiency is proportional to the heat flux and the spray impact area and it is inversely proportional to the mass flow rate and the wall temperature. Two different mass flow rates are being used since two injection pressure are performed in the campaign. An increase in the injection pressure produces a rise in the mass flow rate. All the variables previously described are taking part during the spray-wall interaction influencing the results obtained in the present work. The plume direction angle shows a slightly dependence form stagnation pressure. The average value of tests at 20 MPa is equal to 32.7° and is in good agreement (about 4% error) with the one reported by Payri et al. [47] numerically computed at same testing condition. About the spray cone angle, was found that it varies from 17.3° to 19.5° as it can be seen in Table 3 at the different conditions tested. Numerical results obtained by Payri et al. [48,49] predicts a spray cone angle about 20° at 20 MPa that is in good agreement with T_w = 373 K and 20 MPa present measurement. In the other conditions, the differences can be attributed to the presence of the wall at a small distance from the injector tip and/or the use of spray impact area to estimate this information. The shape of the area of impact for each operating condition are shown in Fig. 11. It is possible to notice that the impact area of the spray rises by increasing the injection pressure and decreases by increasing the temperature of the plate. This overall behavior and the order of magnitude are in agreement with the results shown in [50] for toluene as injected fuel. The condition of higher injection pressure (20 MPa) and lower wall temperature (T_w = 373 K) produces a higher value of major axis of the elliptical like shape spray area of impact, this can be related to the splashing effect of the spray interacting with the wall plus the accumulated amount of non-evaporated liquid which cause a larger footprint.

The spray cooling efficiency maps for all the investigated cases are presented in Fig. 12 by changing the wall temperature and the injection pressure, the heat flux increases as well with a peak in the stagnation point. Also, the efficiency is increased since the impact area is higher due to the splashing phenomenon which is augmented with higher injection pressures. By changing the injection pressure and maintaining the wall temperature constant, the magnitude of the efficiency is practically constant and it is confirmed by the footprint patterns of the plume shown in Fig. 12. On the other hand, by increasing the wall temperature and keeping the injection pressure constant, it is possible to notice an increase in the magnitude of the spray cooling efficiency.

The heat flux shows similar maximum values for the two injection pressures and considerable differences by changing the temperature of the wall, as it can be seen in Figs. 13(a) and 13(b). In the case of the spray cooling efficiency, the overall behavior is similar to the heat flux curves. The higher the wall temperature, the higher is the efficiency, reaching its maximum value at the stagnation point of the spray.

In Figs. 13(a) and 13(b) there is a noticeable difference in the shape of the heat flux and the spray cooling efficiency profiles by changing

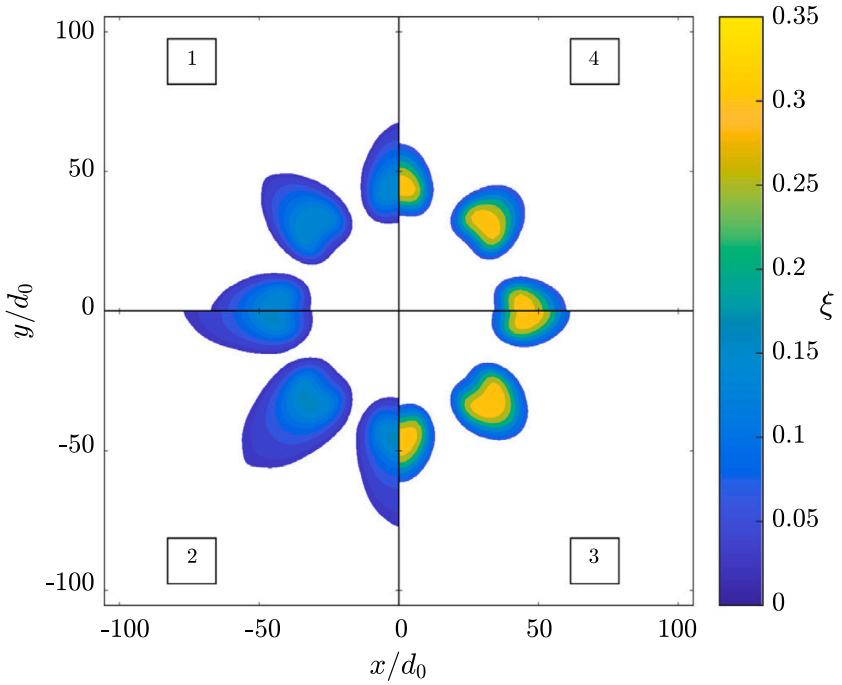

Fig. 12. Spray cooling efficiency. (1) $T_w = 373\,\text{K}, p_{inj} = 10\,\text{MPa}$, (2) $T_w = 373\,\text{K}, p_{inj} = 20\,\text{MPa}$, (3) $T_w = 473\,\text{K}, p_{inj} = 20\,\text{MPa}$, (4) $T_w = 473\,\text{K}, p_{inj} = 10\,\text{MPa}$.

the wall temperature. For the lower wall temperature the shape is wider and presents variability in the falling edge of the curve after the peak value. This is evidence of the splashing phenomenon and the presence of more liquid fuel on the surface of the wall.

5. Conclusions

For the present work, the IR thermography coupled with an inverse heat transfer data reduction was applied to investigate the spray/wall interaction using the "Spray G" injector and iso-octane as the injected fuel. The effect of the injection pressure and the wall temperature over the cooling efficiency, the area of impact and the heat flux of the injector located at 11 mm over a heated thin foil was investigated.

Four cases were taken into account, including two injection pressures (10 and 20 MPa) and two wall temperatures (373 and 473 K). High resolved 2D-heat flux-spray cooling efficiency and area of impact maps were evaluated for each condition. The time-history of the wall spray cooling was reconstructed by a single-image acquisition delayed with respect to the start of the injection by making use of 125 repetitions of the injection event.

Results show that for the lower wall temperature ($T_w = 373K$) the injection pressure has a major effect over the spray impact area, and this is in accordance to the literature. Furthermore, an increase in the wall temperature leads to a reduction in the spray area of impact (due to the fluid vaporization) and a raise in the maximum value of the spray cooling efficiency and the heat flux.

Higher wall temperatures lead to higher fuel vaporization. An increase in the injection pressure enhances the splashing phenomenon which is more evident for the lower wall temperature.

The results show that proposed experimental methodology is an interesting technique to investigate the spray/wall interaction and it can measure wall heat flux distributions, the spray area of impact and spray angles. Used in conjunction with more classical optical techniques such as Schlieren and Diffused Background Illumination can contribute to more robust and comparable results.

The data acquired along this work will be also useful to focus further investigations in the fuel-rich zones after the spray impingement to achieve a better understanding of soot emissions, fuel film adhesion, and the spray spreading on a hot wall.

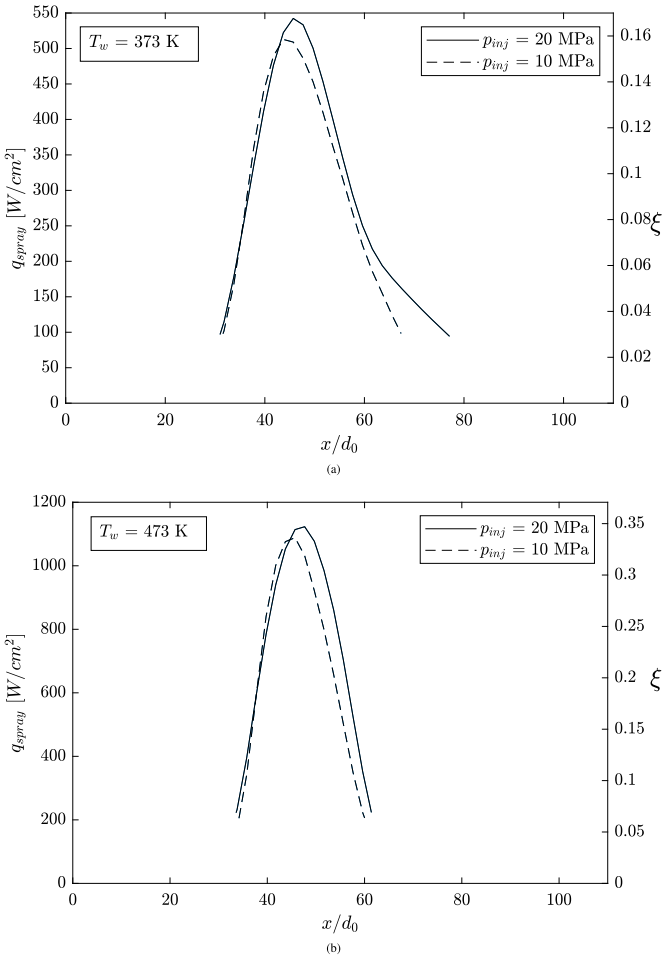

Fig. 13. Spray cooling efficiency and heat flux spatial distribution along the symmetry axis of a single plume.

CRediT authorship contribution statement

Mirko Zaccara: Writing – original draft, Writing – review & editing, Supervision, Software, Investigation, Data curation, Methodology, Formal analysis, Visualization. **César Carvallo:** Writing – original draft, Writing – review & editing, Investigation, Software, Formal analysis, Visualization, Data curation. **Alessandro Montanaro:** Conceptualization, Methodology, Supervision, Project administration, Resources, Writing – review & editing. **Jaime Gimeno:** Review & editing, Supervision. **Luigi Allocca:** Conceptualization, Methodology, Supervision, Project administration, Resources, Writing – review & editing. **Gennaro Cardone:** Conceptualization, Methodology, Supervision, Project administration, Writing – review & editing, Software, Validation, Formal analysis, Resources, Visualization, Data curation.

Declaration of competing interest

The authors declare that they have no known competing financial interests or personal relationships that could have appeared to influence the work reported in this paper.

Data availability

Data will be made available on request.

Acknowledgments

The author C. Carvallo thanks the Universitat Politècnica de València for his predoctoral contract (FPI-2019- S1) which is included within the framework of Programa de Apoyo para la Investigación *y* Desarrollo (PAID-01-19) and would also like to say thanks for the mobility economical help provided by the program "Ayudas para movilidad dentro del Programa para la Formación de Personal investigador (FPI) de la UPV".

The authors kindly acknowledge Consiglio Nazionale delle Ricerche - STEMS for hardware and technical support.

Funding for open access charge: CRUE-Universitat Politècnica de València

References

[1] J. Tian, M. Zhao, W. Long, K. Nishida, T. Fujikawa, W. Zhang, Experimental study on spray characteristics under ultra-high injection pressure for DISI engines, Fuel 186 (2016) 365–374, http://dx.doi.org/10.1016/j.fuel.2016.08.086, URL https://www.sciencedirect.com/science/article/pii/S0016236116308250.

[2] B. Higgins, D.L. Siebers, Measurement of the Flame Lift-Off Location on DI Diesel Sprays Using OH Chemiluminescence, SAE Paper 2001-01-0918, 2001.

[3] A.L. Kastengren, F.Z. Tilocco, C.F. Powell, J. Manin, L.M. Pickett, R. Payri, T. Bazyn, Engine combustion network (ECN): Measurements of nozzle geometry and hydraulic behavior, At. Sprays 22 (12) (2012) 1011–1052, http://dx.doi.org/10.1615/AtomizSpr.2013006309.

[4] L. Allocca, M. Lazzaro, G. Meccariello, A. Montanaro, Schlieren visualization of a GDI spray impacting on a heated wall: Non-vaporizing and vaporizing evolutions, Energy 108 (2016) 93–98, http://dx.doi.org/10.1016/j.energy.2015.09.107, http://linkinghub.elsevier.com/retrieve/pii/S0360544215013171.

[5] R. Payri, F.J. Salvador, J. Gimeno, J.E. Peraza, Experimental study of the injection conditions influence over n-dodecane and diesel sprays with two ECN single-hole nozzles. Part II: Reactive atmosphere, Energy Convers. Manage. 126 (2016) 1157–1167, http://dx.doi.org/10.1016/j.enconman.2016.07.079.

[6] C. Tropea, M. Marengo, The impact of drops on walls and films, Multiphase Sci. Technol. 11 (1998) 11–36, http://dx.doi.org/10.1615/MultScienTechn.v11.i1.20.

[7] S.Y. Lee, S.U. Ryu, Recent progress of spray-wall interaction research, J. Mech. Sci. Technol. 20 (8) (2006) 1101–1117, http://dx.doi.org/10.1007/BF02916010.

[8] A. Montanaro, M. Migliaccio, L. Allocca, V. Fraioli, S.-y. Lee, A. Zhang, J.D. Naber, Schlieren and Mie Scattering Visualization for Single- Hole Diesel Injector under Vaporizing Conditions with Numerical Validation, SAE Technical Paper, 2014, http://dx.doi.org/10.4271/2014-01-1406.

[9] M. Panao, A. Moreira, Experimental study of the flow regimes resulting from the impact of an intermittent gasoline spray, Exp. Fluids 37 (2004) 834–855, http://dx.doi.org/10.1007/s00348-004-0868-1.

[10] J. Kim, Spray cooling heat transfer: The state of the art, Int. J. Heat Fluid Flow 28 (4) (2007) 753–767, http://dx.doi.org/10.1016/j.ijheatfluidflow.2006.09.003.

[11] A. Moreira, A. Moita, M. Panão, Advances and challenges in explaining fuel spray impingement: How much of single droplet impact research is useful? Prog. Energy Combust. Sci. 36 (5) (2010) 554–580, http://dx.doi.org/10.1016/j.pecs.2010.01.002.

[12] H. Hiroyasu, K. Nishida, Fuel Spray Trajectory and Dispersion in a D.I. Diesel Combustion Chamber, SAE Technical Paper Series, SAE International, 1989, http://dx.doi.org/10.4271/890462.

[13] A. Montanaro, L. Allocca, G. Meccariello, M. Lazzaro, Schlieren and Mie Scattering Imaging System to Evaluate Liquid and Vapor Contours of a Gasoline Spray Impacting on a Heated Wall, SAE Technical Paper Series, SAE International, 2015, http://dx.doi.org/10.4271/2015-24-2473.

[14] A. Montanaro, L. Allocca, G. Meccariello, R. Ianiello, Fuel distribution of a GDI spray impacting on a heated wall: Liquid and vapour phases, in: ICLASS International Conference on Liquid Atomization and Spray Systems, 2018.

[15] K. Sato, T. Tadokoro, M. Yamakawa, H. Yokohata, K. Nishida, Y. Sumoto, J. Tian, Spray and Evaporation Characteristics of Multi-Hole Injector for DISI Engines - Effect of Diverging Angle Between Neighboring Holes, SAE Technical Paper Series, SAE International, 2009, http://dx.doi.org/10.4271/2009-01-1500.

[16] B.S. Higgins, C.J. Mueller, D.L. Siebers, Measurements of Fuel Effects on Liquid-Phase Penetration in DI Sprays, SAE Technical Paper Series, SAE International, 1999, http://dx.doi.org/10.4271/1999-01-0519.

[17] S.A. Skeen, J. Manin, L.M. Pickett, Simultaneous formaldehyde PLIF and high-speed schlieren imaging for ignition visualization in high-pressure spray flames, Proc. Combust. Inst. 35 (3) (2015) 3167–3174, http://dx.doi.org/10.1016/j.proci.2014.06.040.

[18] R. Schmehl, H. Rosskamp, M. Willmann, S. Wittig, CFD analysis of spray propagation and evaporation including wall film formation and spray/film interactions, Int. J. Heat Fluid Flow 20 (5) (1999) 520–529, http://dx.doi.org/10.1016/s0142-727x(99)00041-7.

[19] L. Allocca, S. Alfuso, L. Marchitto, G. Valentino, GDI multi-hole injector: Particle size and velocity distribution for single and jet-to-jet evolution analysis, in: ICLASS International Conference on Liquid Atomization and Spray Systems, 2009.

[20] D. Piazzullo, M. Costa, L. Allocca, A. Montanaro, V. ROCCO, A 3D CFD simulation of GDI sprays accounting for heat transfer effects on wallfilm formation, SAE Int. J. Engines 10 (4) (2017) 2166–2175, http://dx.doi.org/10.4271/2017-24-0041.

[21] F. Schulz, J. Schmidt, F. Beyrau, Development of a sensitive experimental set-up for LIF fuel wall film measurements in a pressure vessel, Exp. Fluids 56 (5) (2015) http://dx.doi.org/10.1007/s00348-015-1971-1.

[22] F. Schulz, W. Samenfink, J. Schmidt, F. Beyrau, Systematic LIF fuel wall film investigation, Fuel 172 (2016) 284–292, http://dx.doi.org/10.1016/j.fuel.2016.01.017.

[23] Y. sheng Cheng, K. Deng, T. Li, Measurement and simulation of wall-wetted fuel film thickness, Int. J. Therm. Sci. 49 (4) (2010) 733–739, http://dx.doi.org/10.1016/j.ijthermalsci.2009.10.006.

[24] ECN, Engine combustion network, 2010, Online URL https://ecn.sandia.gov/.

[25] N.K. Akafuah, A.J. Salazar, K. Saito, Infrared thermography-based visualization of droplet transport in liquid sprays, Infrared Phys. Technol. 53 (3) (2010) 218–226, http://dx.doi.org/10.1016/j.infrared.2009.12.002.

[26] F. Schulz, J. Schmidt, A. Kufferath, W. Samenfink, Gasoline wall films and spray/wall interaction analyzed by infrared thermography, SAE Int. J. Engines 7 (3) (2014) 1165–1177, http://dx.doi.org/10.4271/2014-01-1446.

[27] G.M. Carlomagno, G. Cardone, Infrared thermography for convective heat transfer measurements, Exp. Fluids 49 (6) (2010) 1187–1218, http://dx.doi.org/10.1007/s00348-010-0912-2.

[28] M. Gibbons, A. Robinson, Heat transfer characteristics of single cone-jet electrosprays, Int. J. Heat Mass Transfer 113 (2017) 70–83.

[29] M. Contino, M. Zaccara, A. Montanaro, L. Allocca, G. Cardone, Dynamic thermal behavior of a GDI spray impacting on a heated thin foil by phase-averaged infrared thermography, 2020, http://dx.doi.org/10.4271/2019-24-0036.

[30] D.J. Duke, A.L. Kastengren, K.E. Matusik, A.B. Swantek, C.F. Powell, R. Payri, D. Vaquerizo, L. Itani, G. Bruneaux, R.O. Grover, S. Parrish, L. Markle, D. Schmidt, J. Manin, S.A. Skeen, L.M. Pickett, Internal and near nozzle measurements of engine combustion network "Spray G" gasoline direct injectors, Exp. Therm Fluid Sci. 88 (2017) 608–621, http://dx.doi.org/10.1016/j.expthermflusci.2017.07.015, URL https://www.sciencedirect.com/science/article/pii/S089417771730211X.

[31] J. Manin, Y. Jung, S.A. Skeen, L.M. Pickett, S.E. Parrish, L. Markle, Experimental Characterization of DI Gasoline Injection Processes, SAE Technical Paper Series, SAE International, 2015, http://dx.doi.org/10.4271/2015-01-1894.

[32] M. Moulai, R. Grover, S. Parrish, D. Schmidt, Internal and Near-Nozzle Flow in a Multi-Hole Gasoline Injector Under Flashing and Non-Flashing Conditions, SAE Technical Paper Series, SAE International, 2015, http://dx.doi.org/10.4271/2015-01-0944.

[33] T. Astarita, G.M. Carlomagno, Infrared Thermography for Thermo-Fluid-Dynamics, Springer Berlin Heidelberg, 2013, http://dx.doi.org/10.1007/978-3-642-29508-9.

[34] D.G. Walker, E.P. Scott, Evaluation of estimation methods for high unsteady heat fluxes from surface measurements, J. Thermophys. Heat Transfer 12 (4) (1998) 543–551, http://dx.doi.org/10.2514/2.6374.

[35] T.W. Watson, H.E. Robinson, Thermal conductivity of some commercial iron-nickel alloys, J. Heat Transfer 83 (4) (1961) 403–407, http://dx.doi.org/10.1115/1.3683651.

[36] O. Raghu, J. Philip, Thermal properties of paint coatings on different backings using a scanning photo acoustic technique, Measure. Sci. Technol. (2006).

[37] A.-J.N. Khalifa, Natural convective heat transfer coefficient – A review: I. Isolated vertical and horizontal surfaces, Energy Convers. Manage. 42 (4) (2001) 491–504, http://dx.doi.org/10.1016/S0196-8904(00)00042-X, URL https://www.sciencedirect.com/science/article/pii/S019689040000042X.

[38] T. Coleman, Y. Li, An interior trust region approach for nonlinear minimization subject to bounds, SIAM (1996) 418–445, http://dx.doi.org/10.1137/0806023.

[39] L. de Luca, G. Cardone, D. Aymer de la Chevalerie, A. Fonteneau, Goertler instability of a hypersonic boundary layer, Exp. Fluids 16 (1) (1993) 10–16, http://dx.doi.org/10.1007/BF00188500.

[40] F. Avallone, C.S. Greco, F.F.J. Schrijer, G. Cardone, A low-computational-cost inverse heat transfer technique for convective heat transfer measurements in hypersonic flows, Exp. Fluids 56 (4) (2015) 86, http://dx.doi.org/10.1007/s00348-015-1951-5.

[41] Vende, Trinque, Lacour, Delahaye, Fournaison, Efficiency of water spraying on a heat exchanger: Local characterization with the impacted surface, Appl. Therm. Eng. 128 (2017) 684–695, http://dx.doi.org/10.1016/j.applthermaleng.2017.09.031.

[42] N. Otsu, A threshold selection method from gray-level histograms, IEEE Trans. Syst., Man, Cybern. (1979) doi:10.1109/TSMC.1979.4310076.

[43] National institute of standards and technology, 2021, Online URL https://webbook.nist.gov/cgi/cbook.cgi?ID=C540841&Units=SI&Mask=FFF.

[44] G. Paolillo, C.S. Greco, G. Cardone, Impingement heat transfer of quadruple synthetic jets, Int. J. Heat Mass Transfer 135 (2019) 1192–1206, http://dx.doi.org/10.1016/j.ijheatmasstransfer.2019.02.010, URL https://www.sciencedirect.com/science/article/pii/S0017931018357119.

[45] R. Moffat, Describing the uncertainties in experimental results, Exp. Therm Fluid Sci. (1988) 3–17.

[46] S. Crowder, C. Delker, E. Forrest, N. Martin, Determining uncertainties in fitted curves, in: Introduction to Statistics in Metrology, Springer International Publishing, Cham, 2020, pp. 227–265, http://dx.doi.org/10.1007/978-3-030-53329-8_10.

[47] R. Payri, J. Gimeno, P. Martí-Aldaraví, M. Martínez, Transient nozzle flow analysis and near field characterization of gasoline direct fuel injector using large eddy simulation, Int. J. Multiph. Flow. 148 (2022) 103920, http://dx.doi.org/10.1016/j.ijmultiphaseflow.2021.103920, URL https://www.sciencedirect.com/science/article/pii/S030193222100327X.

[48] R. Payri, J. Gimeno, P. Marti-Aldaravi, M. Martinez, Nozzle Flow Simulation of GDi for Measuring Near-Field Spray Angle and Plume Direction, SAE Technical Paper 128, 2019, p. 11, http://dx.doi.org/10.4271/2019-01-0280.

[49] R. Payri, J. Gimeno, P. Marti-Aldaravi, M. Martinez, Large eddy simulations of the fuel injection and mixing process of the ECN GDi injector spray G, in: ICLASS International Conference on Liquid Atomization and Spray Systems, 2021.

[50] H. Luo, K. Nishida, S. Uchitomi, Y. Ogata, W. Zhang, T. Fujikawa, Effect of temperature on fuel adhesion under spray-wall impingement condition, Fuel 234 (2018) 56–65, http://dx.doi.org/10.1016/j.fuel.2018.07.021.